Radiation Measurements 134 (2020) 106314

Contents lists available at ScienceDirect

Radiation Measurements

journal homepage: http://www.elsevier.com/locate/radmeas

Characterisation and comparison of micropatterns written using a proton beam in Ag-activated glass and LiF crystal observed by single- and multi-photon microscopy

Toshio Kurobori [a,*], Wataru Kada [b], Yuka Yanagida [c], Yasuhiro Koguchi [c], Takayoshi Yamamoto [c], Milko Jakšić [d]

[a] Kanazawa University, Kanazawa, Ishikawa, 920-1192, Japan
[b] Gunma University, Kiryu, Gunma, 376-8515, Japan
[c] Chiyoda Technol Corporation, Oarai, Ibaraki, 311-1313, Japan
[d] Ruđer Bošković Institute, Bijennicka Cesta 54, 10000, Zagreb, Croatia

ARTICLE INFO

Keywords:
Radiophotoluminescence (RPL)
Ag-activated phosphate glass
Lithium fluoride (LiF)
Proton beam writing
Single- and multi-photon microscopes

ABSTRACT

We investigate the characterisation and comparison of micro-scale patterns in silver-activated phosphate glass and lithium fluoride (LiF) single crystal written by a proton beam with an energy range of 1.7–4.5 MeV. A variety of micro-scale structures based on blue and orange luminescent Ag-related colour centres in Ag-activated glass and green and red luminescent F-aggregated colour centres in LiF are visualised by combining single- and two-photon confocal microscopes equipped with a blue continuous wave (cw) laser diode and a femtosecond (fs) laser in the near-infrared (NIR) region, respectively. Two- and three-dimensional (2D and 3D) reconstructed images are analytically evaluated using lateral/axial RPL intensity mapping. In addition, the origins of different RPL intensity profiles in a plateau region along the axial direction in both materials are examined and discussed.

1. Introduction

Silver-activated phosphate glass is the most widely known radiophotoluminescent (RPL) material (Perry, 1987; Yokota and Imagawa, 1966; Yamamoto et al., 2011; Hung and Hsu, 2011; Kurobori et al., 2010; Miyamoto et al., 2011) and can be generally used in personal, environmental and clinical demands. The RPL passive dosimetric detector using Ag-activated glass has certain prominent features: a high spatial resolution, long-term stability against fading, a wide dose range, a high-efficiency RPL, low energy responses, non-destructive readout capability, and good reproducibility. In addition to the use of practical dosimeters having the aforementioned desirable properties of Ag-activated glass, we have tested and successfully developed various applications to verify new possibilities of this material: disk-type X-ray 2D and 3D dose imaging detectors (Kurobori and Nakamura, 2012), fluorescence nuclear track detectors (FNTDs) (Kurobori et al., 2017; Kodaira et al., 2020), focused proton beam micro-scale structures (Kurobori et al., 2018) and a real-time fibre-optic coupled dosimetry system (Kurobori, 2018; Kurobori et al., 2020), using different shapes of RPL Ag-activated glasses.

On the other hand, lithium fluoride (LiF) is of particular interest due to the excellent thermal and optical stabilities of its colour centres (CCs) among the alkali halides even at room temperature, as well as its good physical and chemical properties. In particular, the F_2 and F_3^+ CCs (i.e., two electrons bound to two or three neighbouring anion vacancies, respectively) (Nahum and Wiegand, 1967; Baldacchini et al., 2000) in coloured LiF crystals based on the RPL (Levita et al., 1976; Bilski et al., 2017) are excellent candidates for applications of a distributed feedback (DFB) CC laser (Kawamura et al., 2004), X-ray imaging detectors (Baldacchini et al., 2003; Bonfigli et al., 2005), radiation detectors for proton beam diagnostics (Kurobori and Matoba, 2014; Piccinini et al., 2015; Montereali et al., 2018), proton Bragg curve analysis (Nichelatti et al., 2019), and FNTDs in neutron dosimetry (Bilski et al., 2018).

The proton beam writing (PBW) technique (Watt et al., 2007), which uses a MeV proton beam focused to a typical beam size of 1 μm in diameter (Kamia et al., 2009), possesses several desirable advantages such as the fabrication of high-aspect ratio sub-micron 3D structures; the possibility of high penetration depth with little lateral beam spreading; the possibility of controllable penetration depth by varying only the proton beam energy; and the capability of producing structures with

* Corresponding author.
E-mail address: kurobori@staff.kanazawa-u.ac.jp (T. Kurobori).

https://doi.org/10.1016/j.radmeas.2020.106314
Received 4 October 2019; Received in revised form 27 January 2020; Accepted 11 March 2020
Available online 23 March 2020

high packing density.

With advances in the PBW technique, fluorescence light microscopy has also been improved to visualise such 2D and 3D micro-scale structures, the RPL intensity profiles, and fluorescent spectra written into various materials with higher resolving power (Bonfigli et al., 2016; Zheng and Kurobori, 2011,Zheng et al., 2011). Here, the observation and reconstruction of 2D and 3D micro-scale images were carried out via single- and multi-photon confocal laser scanning microscopes (CLSMs) equipped with a blue cw laser diode and a mode-locked Ti:sapphire fs laser, respectively. In a recent paper (Kurobori et al., 2018), the RPL intensity distributions as a function of the implantation depth for a variety of micro-scale patterns in Ag-activated glasses were measured and a significant broadening, similar to a rectangular depth profile, in a plateau region along the axial direction in the experiment when compared to the SRIM simulation was observed.

In the present paper, two different RPL materials: Ag-activated glass and LiF crystal, having almost similar physical and optical properties were selected and investigated to clarify the origins of the aforementioned significant broadening of the Bragg curve. In addition, whether the broadening was closely related to the excitation wavelengths and the composition of the materials or not and whether each fluorescence lifetime of active CCs was affected by a limited-time of fluorescence intensity stored per pixel in CLSMs or not were systematically examined.

2. Experimental procedure

2.1. Samples

A commercially available optically polished Ag-activated glass plate (GD-450, Chiyoda Technol Co.) and LiF single crystals (Ohyo Koken Kogyo Co.) with dimensions of approximately $8.5 \times 8.5 \times 1.5$ mm^3 were used for the optical measurements and analysis for the 2D and 3D microscope images written by a proton beam. The weight composition of Ag-activated glass was the same as that of FD-7 (AGC Techno Glass), i.e., 31.55% P, 51.16% O, 6.12% Al, 11.00% Na and 0.17% Ag.

2.2. X-rays

X-ray irradiations were performed using an X-ray unit with a copper (Cu) anode target with the Be window operating at a tube voltage of 30 kVp, a current of 10–20 mA and an energy of 8 keV. The X-ray attenuation length in phosphate glass and LiF at the utilised X-ray energy of 8 keV has been calculated (http://henke.lbl.gov/optical_constants/atten2.html) to be ~340 μm and ~325 μm, respectively. The samples were placed at an approximately 7-cm distance from the tube.

2.3. Proton beam writing system

The micro-beam patterning was performed at the TIARA irradiation facilities of QST Takasaki, Japan (Kamia et al., 2015). The proton beam was generated by the single-ended particle accelerator with energies of 1.7 and 3 MeV and then focused to a typical beam size of 1 μm in diameter on the image point. The scanning area of the proton micro-beam was controlled using an electrostatic deflection scanner to be a maximum of 800×800 μm^2. Proton beams were incident perpendicular to the sample surface (8.5×8.5 mm^2 plane). Computer-assisted software was used to precisely control the irradiated position, exposure time, current, fluence and repetition of the scanning. The irradiation fluence was in the range of 10^9 - 10^{10} ions/cm^2. Further details on the system are described elsewhere (Kada et al., 2012; Kawabata et al., 2016).

In addition, the micro-beam with an energy of 4.5 MeV was employed within the RBI, Zagreb, Croatia, to write the rectangular patterns with a 300×350 μm^2 field of view at different fluences in the range $(1.43–28.9) \times 10^8$ ions/cm^2 (the irradiation time approximately 10, 30, 100, and 300 s for a fluence rate of 1.43×10^7 ions/s/cm^2) under simultaneous exposure conditions within the Ag-activated glasses and LiF crystals. The corresponding absorption doses can be estimated to be approximately 8.7 Gy for marked-1 and 177 Gy for marked-4, as shown in Fig. 4a.

2.4. Steady- and transient-state spectra

The steady-state optical absorption (OA) spectra were determined at room temperature using a Hitachi U–3900H spectrophotometer with a 1-nm step. The emission (RPL) spectra were acquired using a combination of a high-repetition-rate Q-switched laser (Explorer One, Spectra Physics) at 349 nm for Ag-activated glasses and a picosecond laser (QuixX445-100PS, Omicron-Laserage Laserprodukte GmbH) at 445 nm for LiF crystals, a photonic multichannel analyser (PMA-12, Hamamatsu Photonics) and a delay/pulse generator (DG535, Stanford Research Systems). The pulse duration of the laser was less than 5 ns (full-width at half-maximum, FWHM) for the former and 500 ps for the latter at a repetition rate of 1 kHz for a pulse energy of less than 1 μJ at the sample. Here, the blue and orange RPL signals in Ag-activated glass and green and red RPL signals in LiF were acquired through a long-pass filter passing all wavelengths longer than 400 nm (#84–754, Edmund Optics) and 450 nm (#84–755, Edmund Optics), respectively. Further details on the system are described elsewhere (Kurobori et al., 2016).

2.5. Single- and multi-photon confocal microscopy

For the observation of a variety of micro-scale patterns, a single-photon confocal microscope (A1R, Nikon Instech) equipped with a blue cw laser diode operating at 405 nm was used for both materials, although a 405-nm laser line was not suitable for the excitation source (Kurobori et al., 2016). On the other hand, a multi-photon confocal microscope (A1R MP+, Nikon Instech) equipped with a mode-locked Ti:sapphire laser was used as a two-photon excitation source. The excitation wavelengths at 720 and 890 nm were tuned to excite both Ag^{2+} and Ag^0 CCs at approximately 360 nm in irradiated Ag-activated glass and both F_2 and F_3^+ CCs at 445 nm in irradiated LiF, respectively. The average output power was less than 10 mW at the sample. For single-and multi-photon CLSMs, two objective lenses (Nikon Plan Apo) with different magnifications and numerical apertures (NA) were used: the applied configurations were 20 × /0.75NA and 40 × /1.15NA. The blue and orange RPL signals in Ag-activated glass were acquired via single- and multi-photon CLSMs using a short-pass (SP) filter at 492 nm and a long-pass (LP) filter passing all wavelengths longer than 568 nm, respectively. In the case of LiF, the green and red RPL signals were acquired using band-pass (BP) filters at 525 ± 50 nm and 595 ± 50 nm, respectively, for a single-photon CLSM. For a multi-photon CLMS, 500LP/560SP filters for the green signal and a 568 LP filter for the red signal were used.

3. Results and discussion

Fig. 1 presents OA spectra, including the background (BG) of (Fig. 1a) Ag-activated glass and (Fig. 1b) LiF crystal after X-ray irradiation operating at a tube voltage of 30 kV and a current of 10 mA for 10 min for the former and a current 20 mA for 60 min for the latter at the same position from the tube. In the case of Fig. 1a, several absorption peaks (Ag_3^+ or Ag_3^{2+}) at 4.92 eV, Ag_2^+ at 4.59 eV, Ag^{2+} at 4.00 eV, Ag^0 at 3.44 eV, and phosphorus-oxygen-hole centres (POHCs) at 2.25 eV can be seen; these bands have been identified in previous papers using the strong analogy with Ag-doped NaCl (Kurobori et al., 2010), RPL decay curve analysis, peak fitting analysis, and heat treatments (Zheng and Kurobori, 2011, Zheng et al., 2011). On the other hand, in the case of Fig. 1b, F_3 (R_1) at 3.97 eV, F_3 (R_2) at 3.30 eV, F_2 at 2.79 eV, F_3^+ at 2.77 eV, and F_4 (N_2) at 1.9 eV can be observed and have been identified in previous papers (e.g., Bonfigli et al., 2005). The upward and downward arrows indicate that each peak absorption band increases or decreases

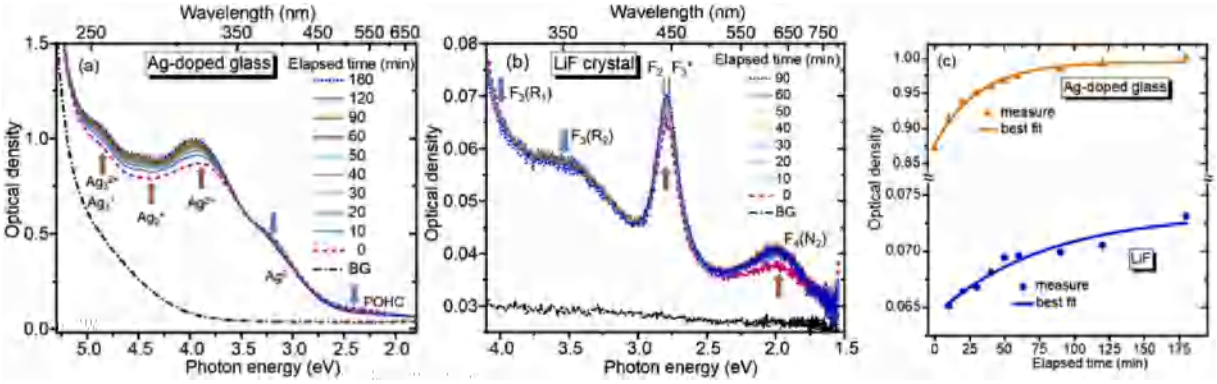

Fig. 1. (Colour online) Optical absorption spectra of the (a) Ag-activated glass and (b) LiF after X-ray-irradiation. Several X-ray-induced absorption bands are marked. The upward and downward arrows indicate that each peak absorption band increases or decreases as a function of elapsed time. (c) The build-up curves for Ag^{2+} centres in Ag-activated glass and M centres in LiF. (For interpretation of the references to colour in this figure legend, the reader is referred to the Web version of this article.)

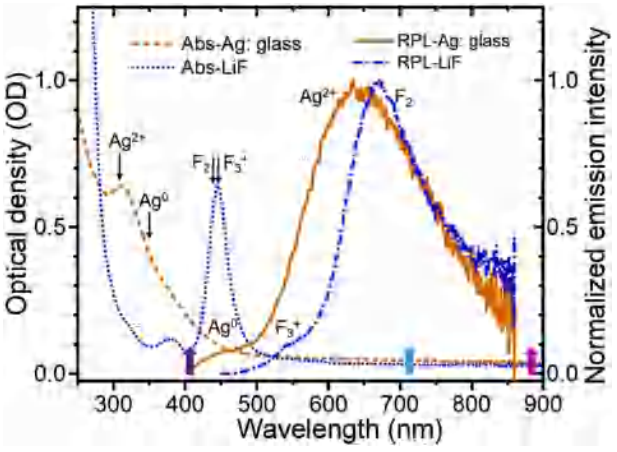

Fig. 2. (Colour online) Optical absorption spectra and normalised RPL spectra the Ag-activated glass and LiF after X-ray irradiation. Several dominant bands for the measurements are marked. The laser lines for 1 PE and 2 PE are indicated by the thick vertical arrows: 405, 720 and 890 nm. (For interpretation of the references to colour in this figure legend, the reader is referred to the Web version of this article.)

with increasing time from 0 (just-irradiation) to 180 min for the Ag-activated glass and 90 min for LiF after X-ray irradiations.

Similar phenomena were also observed in RPL spectra (not shown here) after stimulating each band. This phenomenon is representative of a characteristic RPL "build-up" curve of the Ag-activated phosphate glass, i.e., the RPL centre concentration, especially attributed to Ag^{2+} centres, increases slowly as a function of elapsed time both during and after irradiation (e.g., Perry, 1987; Dmitryuk et al., 1996; Miyamoto et al., 2011; Kurobori, 2018; Kurobori et al., 2020; McKeever et al., 2019; 2020). The (Ag_3^+ or Ag_3^{2+}), Ag_2^+ and Ag^{2+} centres in the Ag-activated glass and F_2, F_3^+ and F_4 (N_2) centres in LiF show the inevitable "build-up" phenomena. Fig. 1c shows the "build-up" curve of each peak absorption value for Ag^{2+} centres in the Ag-activated glass and M centres for LiF. The F_2 and F_3^+ CCs in LiF are characterised by nearly completely overlapping absorption bands, as shown in Fig. 1b, with maxima near 445 nm (known as a whole as the M band) (Nahum and Wiegand, 1967). The build-up curves for the absorption spectra after X-ray irradiation were fitted to a single exponential plus a constant. In these cases, the R^2-values were $R^2 = 0.986$ and 0.946 for Ag-activated glass and LiF, respectively.

Note that the optical density (OD) value of LiF is much lower than that of the Ag-doped glass, although the absorbed dose for LiF (X-ray exposure: 30 kV, 20 mA, for 60 min) is much higher than that of the Ag-doped glass (X-ray exposure: 30 kV, 10 mA, for 10 min). Therefore, a LiF dosimeter was developed that can be used at higher doses from 10^1 to 10^5 Gy (Montereali et al., 2018). In contrast, an Ag-activated glass dosimeter can be used at lower doses from several tens of μGy to 10 Gy (Miyamoto et al., 2011). In general, the RPL glass dosimetry is subjected to preheating at 70 °C for 30 min for practical utilisation to accelerate the "build-up" growth and to acquire the accurate absorbed doses.

As noted, the dose linearity range of an RPL Ag-activated glass dosimeter is 20 μGy–30 Gy at most, but the response may be linear up to 10^3 Gy by suppressing less fluorescence with the use of a devised readout geometry (Barr et al., 1961). Recently, a possibility to extend the dose range was pointed out by the combination of RPL and OA signals. In addition, the dynamic range of the dose was also extended from 10 μGy to 10 kGy by applying this combination to the gamma-ray irradiated Ag-activated glass (Kodaira et al., 2018). Furthermore, Sholom and McKeever (2020) reported on new possibilities of this material used as a high dose electron paramagnetic resonance (EPR)/optical absorption (OA) dosimeter in the range up to several hundreds of kGy.

The physical (mass density, photon effective atomic number, and refractive index) and optical characterisation of Ag-activated glass and LiF crystal obtained in this work are summarised in Table 1. Concerning to the lifetime values, each value was cited from the paper for LiF single crystals (Kurobori et al., 1988) and Ag-activated phosphate glasses (Kurobori et al., 2010), respectively.

The relationship between the absorption spectra and normalised RPL spectra of Ag-activated glass and LiF after X-ray irradiation is shown in Fig. 2. Several dominant bands used here for the measurements of excitation and emission spectra are marked: Ag^{2+} and Ag^0 in the Ag-activated glass and F_2 and F_3^+ in LiF. In addition, the laser lines used to excite these bands via single-photon excitation (1 PE) at 405 nm and two-photon excitation (2 PE) at 720 and 890 nm are indicated by the thick vertical arrows, which correspond to twice the wavelengths of the one-photon absorption of the Ag-activated glass at approximately 360 nm and LiF at 445 nm, respectively.

Table 2 shows the expected lateral (x, y)/axial (z) resolution for one- and two-photon configurations in the Ag-activated glass and LiF crystal using the objective lens with a magnification and numerical aperture (NA), i.e., 40 × /1.15NA. The lateral theoretical resolution of the used objective (40 × /1.15NA) in the Ag-doped glass and LiF for one- and two-photon-wavelengths was calculated (e.g., Diaspro, 2002; Bonfigli et al., 2016) using the equation $r_{xy} \sim 0.46\lambda/NA$, where λ is the excitation wavelength for the one-photon configuration ($\lambda_{exc} = 405$ nm) and the two-photon configuration ($\lambda_{exc} = 720$ and 890 nm). On the other hand, the axial resolution for both materials for one- and

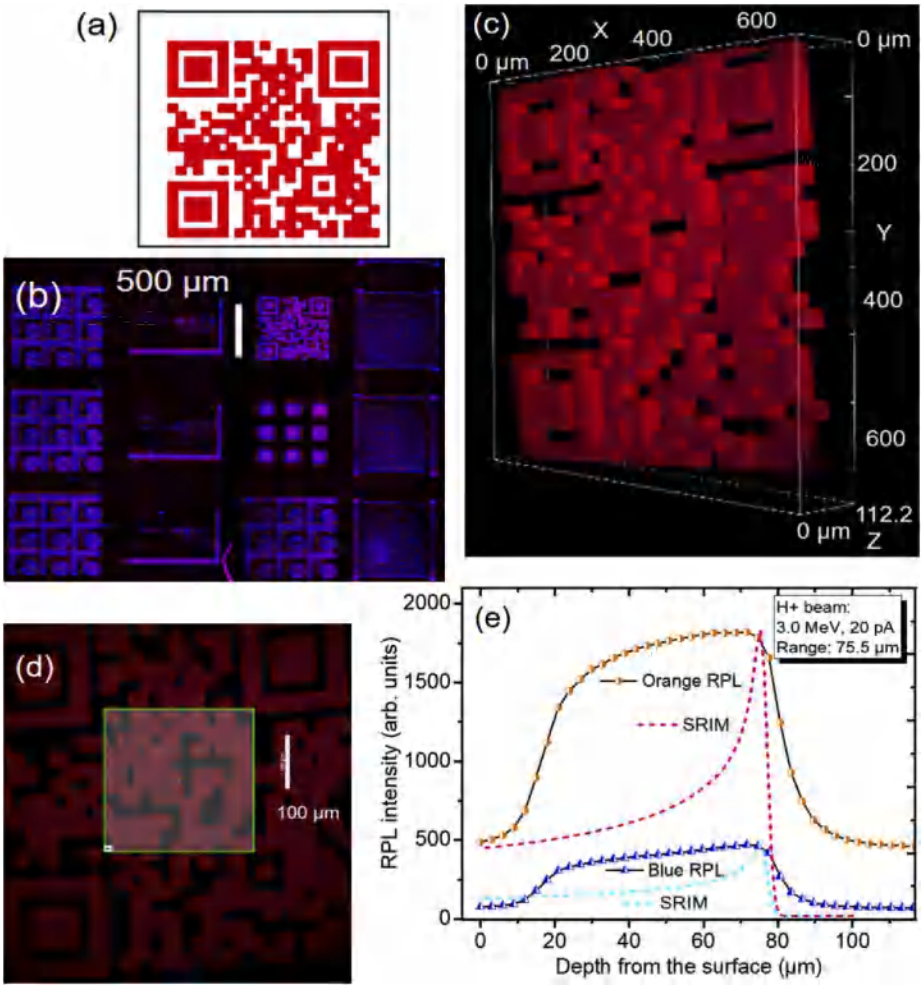

Fig. 3. (Colour online) (a) Original input QR code and (b) a photograph of a variety of micro-scale patterns in Ag-activated glass written by a 3.0 MeV focused proton beam. (c) 3D image of the QR code pattern visualised using a 2 PE (at 720 nm) CLSM (20 × objective, NA = 0.75) (d) 2D image of the QR code pattern and the setting area of region of interest (ROI) used for the analysis. (e) Orange and blue RPL intensity depth profiles along the axial direction and the normalised SRIM-simulation. (For interpretation of the references to colour in this figure legend, the reader is referred to the Web version of this article.)

two-photon-wavelengths was also calculated using the equation $r_z \sim 1.4n\lambda/(NA)^2$, where n is the refractive index of the materials.

Fig. 3a shows a pre-populated QR code used in this work, whose Excel data were transmitted to the scanning electrodes of the proton beam writing system via D/A converters to write arbitrary patterns on the target and Fig. 3b shows a photograph of a variety of micro-scale patterns that were written on the near surface in the Ag-activated glass by a focused proton beam with energies of 3.0 and 1.7 MeV. An intense orange RPL under UV light excitation was observed with the naked eye. It should be highlighted that the typical surface spot size with an energy of 1.7 MeV was approximately 1 × 1 μm^2, which was evaluated using a secondary electron image of a Cu mesh taken before each irradiation experiment, but each dot image of the surface spot size reconstructed using the 100 × /NA1.40, oil immersion (n = 1.515) objective lens configuration was approximately 3× 8 μm^2. In addition, the reconstructed surface spot size of 3 × 8 μm^2 was gradually enlarged from spot sizes of 3.3 × 8.5 μm^2 at a depth of 2.21 μm–8.1 × 10.6 μm^2 at a depth of 10.46 μm (not shown here).

Fig. 3c shows a 3D QR code micro-scale pattern written with an energy of 3.0 MeV and a current of 20 pA (average value) with a 679.5 × 679.5 μm^2 field of view and a total of approximately 47 layers separated by increments of 2.39 μm at depths ranging from 0 to ~112.2 μm below the surface. The images were acquired and reconstructed using the two-photon excitation (at 720 nm) CLSM instrument with a 20 × /0.75NA objective lens configuration. Fig. 3d presents a typical 2D image of the QR code-pattern. The regions of interest (ROI) were set in the constructed image. Fig. 3e presents the RPL intensity profile along the axial direction perpendicular to the surface obtained by the image analysis method for the orange and blue RPL. Since the projected range (or penetration depth) depends on the beam energy, the 3.0 MeV proton beam used here stopped at the estimated range (~75.5 μm depth) in the Ag-activated glass, which was calculated using the SRIM software (Ziegler et al., 2010). Note that a significant broadening, similar to a rectangular depth profile, as shown in Fig. 3e, in a plateau region was observed in the experiment when compared to the SRIM simulation. In addition, note that the total proton exposure times to fabricate such patterns ranged from approximately several seconds to several tens of seconds per pattern.

Fig. 4 show the RPL intensity profiles as a function of depth from the surface for LiF (Fig. 4a) and Ag-activated glass (Fig. 4b). The inset shows a photograph of the rectangular pattern with a 300 × 350 μm^2 field of view with different fluences in the range written by 4.5 MeV proton beams: marked-1 1.43 × 10^8, marked-2 4.29 × 10^8, marked-3 1.43 × 10^9 and marked-4 4.29 × 10^9 ions/cm^2. The 2 PE wavelengths were 890 nm for LiF and 720 nm for Ag-activated glass. For a two-photon microscopy, each axial resolution was approximately 1.31 (Fig. 4a) and 1.16 (Fig. 4b) μm for a 40 × /1.15NA objective lens configuration. The Bragg peak of ~144 μm for LiF and ~148 μm for Ag-activated glass for 4.5 MeV proton energy were in good agreement with the SRIM-simulation, but it should be highlighted that in the case of the Ag-activated glass, a significant broadening similar to a rectangular depth profile for the same 300 × 350 μm^2 field of view and the Bragg peak with large variance inferred from that of LiF were observed.

Fig. 5 shows the proton Bragg curves for the green RPL intensity in LiF as a function of depth from the surface. The Bragg profiles were measured using 1 PE at 405 nm microscope with a 40 × /1.15NA

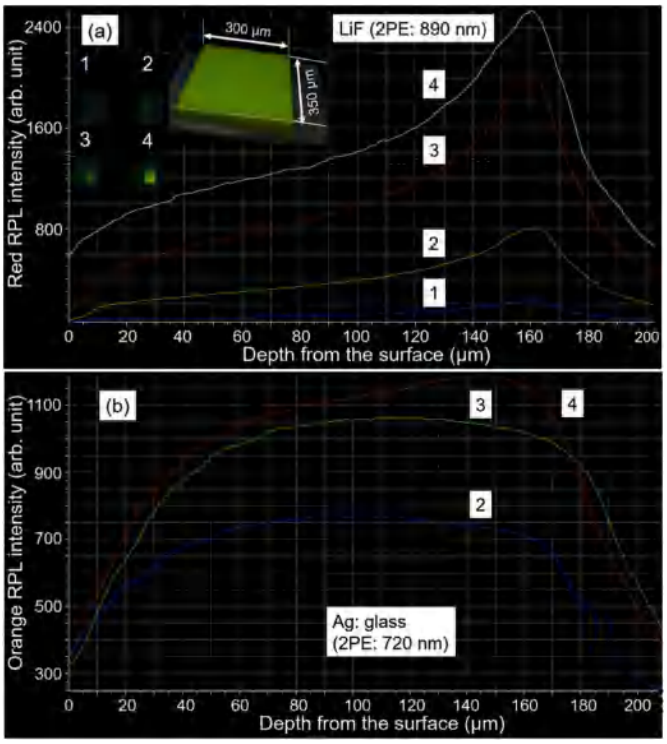

Fig. 4. (Colour online) Red and orange RPL intensity Bragg curves as a function of depth from the surface for (a) LiF and (b) the Ag-activated glass, respectively. The inset shows a photograph of the rectangular pattern with a 300 × 350 μm^2 field of view with different fluences (marked-1 through marked-4) in the range of (1.43–42.9) × 10^8 ions/cm^2. These images were written by the 4.5 MeV proton beam and acquired using a 40 × /1.15NA objective lens. The 2 PE wavelengths were 890 nm for LiF and 720 nm for the Ag-activated glass. (For interpretation of the references to colour in this figure legend, the reader is referred to the Web version of this article.)

Table 1
The physical and optical characterisation of the Ag- activated glass and LiF crystal obtained in this work.

Materials		Ag-doped glass		LiF crystal
mass density (gcm^{-3})		2.61		2.64
effective atomic number		12.57		8.3
refractive index		1.52		1.39
Active centres	Ag^0	Ag^{2+}	F_3^+	F_2
excitation (nm)	360	315	448	444
emission (nm)	460	650	540	680
lifetime (ns)	~5	~2400	~8	~18

Table 2
The expected lateral (x, y)/axial (z) resolution for one- and two-photon configurations for the Ag-activated glass and LiF crystal.

	Type	λ_{exc} (nm)	N	40X (NA)	Lateral r_{xy} (nm)[a]	Axial r_z (nm)[b]
Ag-doped glass	Confocal	405	1.52	1.15	162	652
	2-Photon	720	1.52	1.15	288	1159
LiF crystal	Confocal	405	1.39	1.15	162	596
	2-Photon	890	1.39	1.15	356	1310

[a] r_{xy}~0.46λ/NA.
[b] r_z~1.4nλ/NA^2.

objective lens configuration and were acquired using a BP-filter (525 ± 50 nm). The marked-1 through marked-4 present the rectangular patterns written by the 4.5 MeV proton beam with a 300 × 350 μm^2 field of view at different fluences, as shown in the inset of Fig. 4a. Each green RPL intensity profile with small variance at the Bragg peak position depth obtained by 1 PE at 405 nm was very similar to that of the red intensity profiles in Fig. 4a obtained by 2 PE at 890 nm, although the green RPL intensity obtained using 1 PE was lower than that of the red RPL intensity obtained using 2 PE.

On the other hand, Fig. 6a and b were measured using 1 PE at 405 nm and 2 PE at 720 nm microscopes with a 20 × /0.75NA objective lens configuration, which were acquired using a BP filter (450 ± 25 nm) (blue region) and a LP filter 561 nm (orange region), respectively. The marked-1, -2 and -4 present the rectangular patterns written by the 4.5 MeV proton beam with a 300 × 350 μm^2 field of view at different fluences. The penetration range is in good agreement for 2 PE with a Bragg peak of ~148 μm in the Ag-activated glass. It should be highlighted that in the case of 1 PE, an exceptional broadening with large variance at the Bragg peak position depth was observed.

The experimental results obtained from Figs. 4–6 using the Ag-activated glass and LiF crystal indicate that the origin of an obvious broadening only for the Ag-activated glass may be considered as follows:

(1) The differences in the fluorescence lifetimes between LiF (τ ~18 ns) for red luminescence ascribed to the F_2 centres and the Ag-doped glass (τ ~2400 ns) for orange luminescence ascribed to the Ag^{2+} centres, as shown in Table 1, may be reflected on the dose-depth profiles because the limited time of fluorescence intensity stored per pixel in CLSMs for applying luminescent light is several tens of μs in this work, so the integrated RPL intensity is immediately saturated for the Ag-doped glass. As a result, the dose-depth curve in a plateau region becomes similar to a rectangular profile (c.f. Fig. 4a and b).
(2) Additionally, the experimental results suggest that the origin of the broadening of the Bragg curve is also related to the different centre-formation mechanisms such as F-aggregate centres (i.e. F_2 and F_3^+) in LiF and electron- and hole-trapped Ag-related centres (i.e. Ag^0 and Ag^{2+}) in Ag-activated glass, the different composition of the materials, and the different atomic networks between LiF and Ag-activated phosphate glass.
(3) The multi-proton microscopy (applied to Fig. 4a, b, and Fig. 6b) is more effective than single photon-microscopy (applied to Fig. 5 and 6a): the lack of out-of-focus absorption allows for more of the excitation light to reach the desired sample region; the longer (NIR) wavelength is scattered less than the shorter wavelength, as shown in Fig. 2. In the case of Ag-activated glass, 405 nm (single-photon) light would be expected to undergo approximately ten-fold more scattering than 720 nm (two-photon) light, as predicted by an approximation of Rayleigh scattering. As a result, the effects of fluorescence scattering are less detrimental to two-photon microscopy than to one-photon microscopy (c.f. Fig. 6a and b).

4. Conclusions

The data obtained in this study led to the following conclusions:

(1) A variety of micro-scale patterns (in this work, QR code), which can be controllable penetration depth by varying only the proton beam energy, in Ag-doped glass written using focused-proton beams as small as 1 μm in diameter with energies of 1.7 and 3.0 MeV were observed and demonstrated using multi-photon microscopy (λ_{exc} = 720 nm), as shown in Fig. 3.
(2) The RPL intensity profiles having different fluences with approximately from 8.7 to 177 Gy written using a 4.5 MeV proton beam were observed and compared with each other via one- and

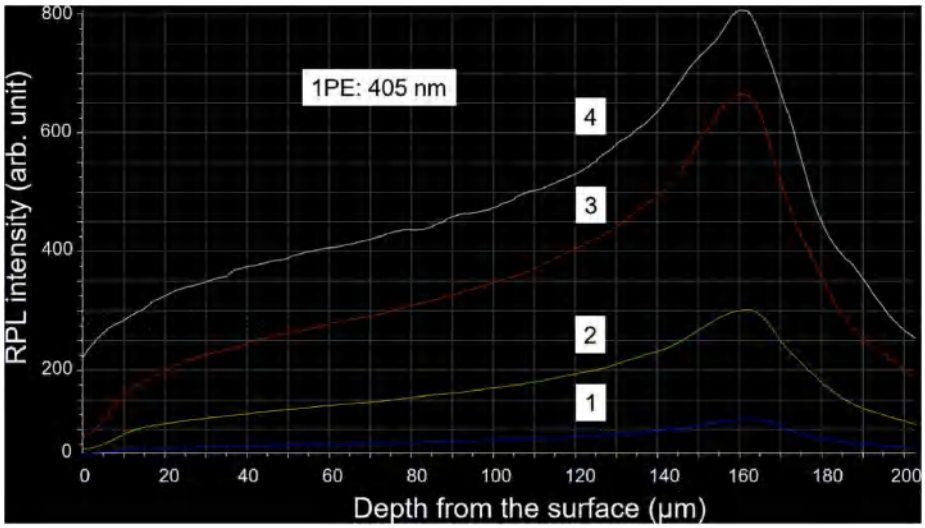

Fig. 5. (Colour online) Bragg curves for the green RPL intensity as a function of depth from the surface visualised using a 1 PE at 405 nm microscope (40 × objective, NA = 1.15). These profiles were written by the 4.5 MeV proton beam. (For interpretation of the references to colour in this figure legend, the reader is referred to the Web version of this article.)

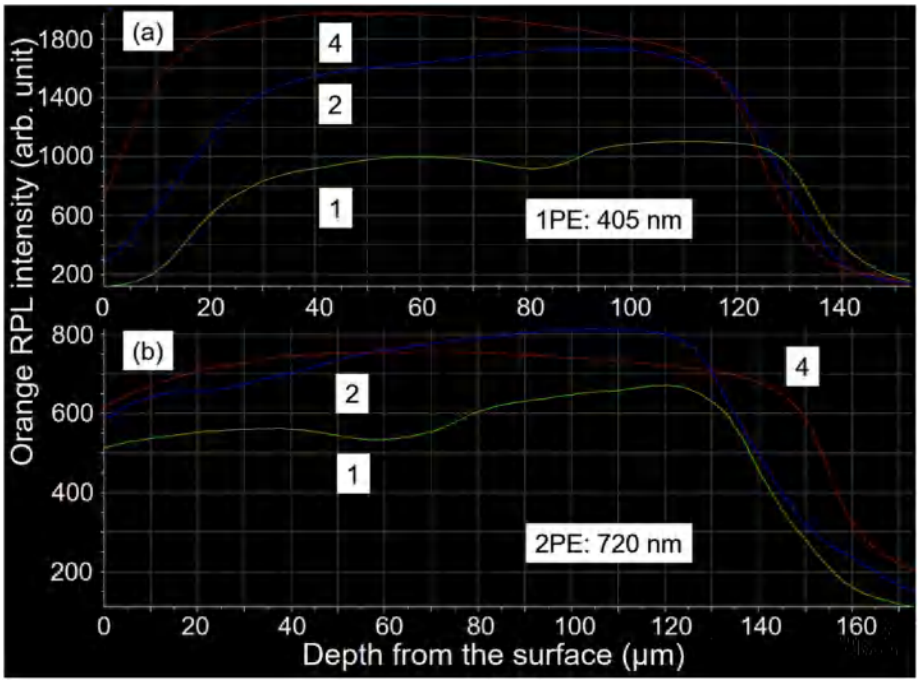

Fig. 6. (Colour online) Bragg curves for the orange RPL intensity as a function of depth from the surface visualised using (a) 1 PE at 405 nm and (b) 2 PE at 720 nm microscopes (20 × objective, NA = 0.75). These images were written by the 4.5 MeV proton beam. (For interpretation of the references to colour in this figure legend, the reader is referred to the Web version of this article.)

two-photon microscopes for the Ag-activated glass and LiF crystal. Even though the same rectangular pattern with a 300 × 350 μm^2 field of view, an outstanding RPL intensity broadening in a plateau region along the axial direction was only observed in Ag-activated glass, as shown in Fig. 4b and Fig. 6.

(3) In addition, the rectangular pattern of the green (attributed to the F_3^+ centres) and red (F_2 centres) RPL in LiF single crystal was visualised almost the same profiles with very small variance at the Bragg peak position for different fluences, regardless of single- and two-photon excitation, as shown in Fig. 4a and 5.

(4) The possible speculation for the significant broadening of the Bragg curve for Ag-doped glass was discussed through the various measurements.

Finally, the developed system in this work combining fabrication of sub-microscale structures in dosimetric transparent materials such as Ag-activated glass and LiF using a focused proton beam and with visualisation of two-photon confocal microscopy using a NIR fs laser should be particularly suitable not only for novel dosimetric applications, but also for practical integrated optical device applications.

Acknowledgements

T. K. would like to thank Prof. H. Nanto at the Kanazawa Institute of Technology for valuable discussions and the staff of Chiyoda Technol Corporation for their contributions in the form of insightful discussions and sample preparation. Furthermore, T.K. would like to thank T. Shirao at the Bio Science Sales Division of Nikon Instech Co., Ltd. for his technical imaging support. This work was supported by JSPS KAKENHI Grant Number 17H03519. We are grateful for the helpful comments and valuable suggestions of two anonymous referees.

References

Baldacchini, G., Nicola, E. De, Montereali, R.M., Scacco, A., Kalinov, V., 2000. Optical bands of F_2 and F_3^+ centers in LiF. J. Phys. Chem. Solid. 61, 21–26. https://doi.org/10.1016/S0022-3697(99)00236-X.

Baldacchini, G., Bonfigli, F., Faenov, A., Flora, F., Marolo, T., Montereali, R.M., Pace, A., Pikuz, T., Reale, L., 2003. Lithium fluoride as a novel X-ray image detector for biological μ-world capture. J. Nanosci. Nanotechnol. 3, 483–486. https://doi.org/10.1166/jnn.2003.023.

Barr, N.F., Stark, M.B., Hands, J., Laughlin, J.S., 1961. Dosimetry with small silver-activated glass rods. Health Phys. 7, 48–53.

Bilski, P., Marczewska, B., Zhydachevskii, Y., 2017. Radiophotoluminescence spectra of lithium fluoride TLDs after exposures to different radiation modalities. Radiat. Meas. 97, 14–17. https://doi.org/10.1016/j.radmeas.2016.12.014.

Bilski, P., Marczewska, B., Kłosowski, M., Gieszczyk, W., Nowak, T., Naruszewicz, M., 2018. Detection of neutrons with LiF fluorescent nuclear track detectors. Radiat. Meas. 116, 35–39. https://doi.org/10.1016/j.radmeas.2018.06.022.

Bonfigli, F., Faenov, A., Flora, F., Marolo, T., Montereali, R.M., Nichelatti, E., Pikuz, T.A., Reale, L., Baldacchini, G., 2005. Point defects in lithium fluoride films for micro-radiography, X-ray microscopy and photonic applications. Phys. Status Solidi 202, 250–255. https://doi.org/10.1002/pssa.200460236.

Bonfigli, F., Hampai, D., Dabagov, S.B., Montereali, R.M., 2016. Characterization of X-ray polycapillary optics by LiF crystal radiation detectors through confocal fluorescence microscopy. Opt. Mater. 58, 398–405. https://doi.org/10.1016/j.optmat.2016.06.012.

Diaspro, A., 2002. Confocal and two-photon microscopy. In: Diaspro, A. (Ed.), Foundations, Applications and Advances. Wiley-Liss, New York.

Dmitryuk, A.V., Paramzina, S.E., Perminov, A.S., Solov'eva, N.D., Timofeev, N.T., 1996. The influence of glass composition on the properties of silver-doped radiophotoluinescent phosphate glasses. J. Non-Cryst. Sol. 202, 173–177. http://henke.lbl.gov/optical_constants/atten2.html.

Huang, D.Y.C., Hsu, S.M., 2011. Radio-Photoluminescence glass dosimeter (RPLGD). In: Gali-Muhtasib, Hala (Ed.), Advances in Cancer Therapy. InTech Open, pp. 553–568.

Kada, W., Yokoyama, A., Koka, M., Takano, K., Satoh, T., Kamiya, T., 2012. Ion-beam-Induced luminescence analysis as diagnostic tool for microstructure patterning on diamond by proton beam writing. Jpn. J. Appl. Phys. 51 https://doi.org/10.1143/JJAP.51.06FB07, 06FB07.

Kamia, T., Takano, K., Ishii, Y., Satoh, T., Oikawa, M., Ohkubo, T., Haga, J., Nishikawa, H., Furuta, Y., Uchiya, N., Seki, S., Sugimoto, M., 2009. Fabrication of nanowires by varying energy microbeam lithography using heavy ions at the TIARA. Nucl. Instrum. Methods Phys. B 267, 2317–2320. https://doi.org/10.1016/j.nimb.2009.03.043.

Kamiya, T., Satoh, T., Koka, M., Kada, W., 2015. Development of microbeam technology to expand applications at TIARA. Nucl. Instrum. Methods Phys. B 348, 4–7. https://doi.org/10.1016/j.nimb.2014.12.047.

Kawabata, S., Kada, W., Parajuli, R.K., Matsubara, Y., Sakai, M., Miura, K., Satoh, T., Koka, M., Yamada, N., Kamiya, T., Hanaizumi, O., 2016. In situ ion-beam-induced luminescence analysis for evaluating a micrometer-scale radio-photoluminescence glass dosimeter. Jpn. J. Appl. Phys. 55, 06GD03 https://doi.org/10.7567/JJAP.55.06GD03.

Kawamura, K., Hirano, M., Kurobori, T., Takamizu, D., Kamiya, T., Hosono, H., 2004. Femtosecond-laser-encoded distributed-feedback color center laser in lithium fluoride single crystals. Appl. Phys. Lett. 84, 311–313. https://doi.org/10.1063/1.1640784.

Kodaira, S., Yanagida, Y., Koguchi, Y., Kawashima, H., Kurano, M., Ogura, K., 2018. Note: complementary approach for radiation dosimetry with Ag^+-activated phosphate glass. Rev. Sci. Instrum. 89, 116106. https://doi.org/10.1063/1.5058697.

Kodaira, S, Kusumoto, T, Kitamura, H, Yanagida, Y, Koguchi, Y, 2020. Characteristics of fluorescent nuclear track detection with Ag^+-activated phosphate glass. Radiat. Meas. 132, 106252. https://doi.org/10.1016/j.radmeas.2020.106252.

Kurobori, T., Kanasaki, T., Imai, Y., Takeuchi, N., 1988. Lifetimes of some excited F-aggregate centres in LiF. J. Phys. C Solid State Phys. 21, L397–L402. https://doi.org/10.1088/0022-3719/21/12/009.

Kurobori, T., Zheng, W., Miyamoto, Y., Nanto, H., Yamamoto, T., 2010. The role of silver in the radiophotoluminescent properties in silver-activated phosphate glass and sodium chloride crystal. Opt. Mater. 32, 1231–1236. https://doi.org/10.1016/j.optmat.2010.04.004.

Kurobori, T., Nakamura, S., 2012. A novel disk-type X-ray area imaging detector using radiophotoluminescence in silver-activated phosphate glass. Radiat. Meas. 47, 1009–1013. https://doi.org/10.1016/j.radmeas.2012.09.003.

Kurobori, T., Matoba, A., 2014. Development of accurate two-dimensional dose imaging detectors using atomic-scale colour centres in Ag-activated phosphate glass and LiF thin films. Jpn. J. Appl. Phys. 53, 02BD14 https://doi.org/10.7567/JJAP.53.02BD14.

Kurobori, T., Yanagida, Y., Chen, Y.Q., 2016. A three-dimensional imaging detector based on nano-scale silver-related defects in X- and gamma-ray-irradiated glasses. Jpn. J. Appl. Phys. 55, 02BC01 https://doi.org/10.7567/JJAP.55.02BC01.

Kurobori, T., Yanagida, Y., Kodaira, S., Shirao, T., 2017. Fluorescent nuclear track images of Ag-activated phosphate glass irradiated with photons and heavy charged particles. Nucl. Instrum. Methods Phys. A. 855, 25–31. https://doi.org/10.1016/j.nima.2017.02.057.

Kurobori, T., 2018. Performance characterisation of a real-time fiber dosimetry system using radiophotoluminescent glasses. Jpn. J. Appl. Phys. 57, 106402. https://doi.org/10.7567/JJAP.57.106402.

Kurobori, T., Kada, W., Shirao, T., Satoh, T., 2018. Two-photon excited microscale colour centre patterns in Ag-activated phosphate glass written using a focused proton beam. Jpn. J. Appl. Phys. 57, 1–7. https://doi.org/10.7567/JJAP.57.02CC01, 02CC0.

Kurobori, T, Yanagida, Y, Koguchi, Y, Yamamoto, T, 2020. Variable periodic time operated fibre-coupled dosimetry system using Ag-activated RPL glasses with build-up. Radiat. Meas. 133, 106300. https://doi.org/10.1016/j.radmeas.2020.106300.

Levita, M., Schlesinger, T., Friedland, S.S., 1976. LiF dosimetry based on radiophotoluminescence (RPL). IEEE Trans. Nucl. Sci. 23, 667–674. https://doi.org/10.1109/TNS.1976.4328325.

McKeever, S.W.S., Sholom, S., Shrestha, N., 2019. Observations regarding the build-up effect in radiophotoluminescence of silver-doped phosphate glasses. Radiat. Meas. 123, 13–20. https://doi.org/10.1016/j.radmeas.2019.02.009.

McKeever, S.W.S., Sholom, S., Shrestha, N., Klein, D., 2020. Build-up of radiophotoluminescence (RPL) in Ag-doped phosphate glass in real-time both during and after exposure to ionizing radiation: A proposed model. Radiat. Meas. 132, 106246. https://doi.org/10.1016/j.radmeas.2020.106246.

Miyamoto, Y., Takei, Y., Nanto, H., Kurobori, T., Konnai, A., Yanagida, T., Yoshikawa, A., Shimotsuma, Y., Sakakura, M., Miura, K., Hirano, K., Nagashima, Y., Yamamoto, T., 2011. Radiophotoluminescence from silver-doped phosphate glass. Radiat. Meas. 46, 1480–1483. https://doi.org/10.1016/j.radmeas.2011.05.048.

Montereali, R.M., Ampollini, A., Picardi, L., Ronsivalle, C., Bonfigli, F., Libera, S., Nichelatti, E., Piccinini, M., Vincenti, M.A., 2018. Visible photoluminescence of aggregate colour centres in lithium fluoride thin films for low-energy proton beam radiation detectors at high doses. J. Lumin. 200, 30–34. https://doi.org/10.1016/j.jlumin.2018.04.005.

Nahum, J., Wiegand, D.A., 1967. Optical properties of some F-aggregate centers in LiF. Phys. Rev. 154, 817–830. https://doi.org/10.1103/PhysRev.154.817.

Nichelatti, E., Ronsivalle, C., Piccinini, M., Picardi, L., Montereali, R.M., 2019. An analytical approximation of proton Bragg curves in lithium fluoride for beam energy distribution analysis. Nucl. Instrum. Methods B 446, 29–36. https://doi.org/10.1016/j.nimb.2019.03.026.

Perry, J.A., 1987. RPL Dosimetry: Radiophotoluminescence in Health Physics. Medical Science Series. Adam Hilger, Bristol.

Piccinini, M., Ambrosini, F., Ampollini, A., Picardi, L., Ronsivalle, C., Bonfigli, F., Libera, S., Nichelatti, E., Vincenti, M.A., Montereali, R.M., 2015. Photoluminescence of radiation-induced color centers in lithium fluoride thin films for advanced diagnostics of proton beams. Appl. Phys. Lett. 106, 261108. https://doi.org/10.1063/1.4923403.

Sholom, S., McKeever, S.W.S, 2020. High-dose dosimetry with Ag-doped phosphate glass: applicability test with different techniques,. Radiat. Meas. 132, 106263. https://doi.org/10.1016/j.radmeas.2020.106263.

Watt, F., Breese, M.B.H., Bettiol, A.A., van Kan, J.A., 2007. Proton beam writing. Mater. Today 10, 20–29. https://doi.org/10.1016/S1369-7021(07)70129-3.

Yamamoto, T., Maki, D., Sato, F., Miyamoto, Y., Nanto, H., Iida, T., 2011. The recent investigations of radiophotoluminescence and its application. Radiat. Meas. 46, 1554–1559. https://doi.org/10.1016/j.radmeas.2011.04.038.

Yokota, R., Imagawa, M., 1966. Radiophotoluminescent centers in silver-activated phosphate glass. J. Phys. Soc. Jpn. 23, 1038–1048. https://doi.org/10.1143/JPSJ.23.1038.

Zheng, W., Kurobori, T., 2011. Assignments and optical properties of X-ray-induced colour centres in blue and orange radiophotoluminescent silver-activated phosphate glasses. J. Lumin. 131, 36–40. https://doi.org/10.1016/j.jlumin.2010.08.024.

Zheng, W., Kurobori, T., Miyamoto, Y., Nanto, H., Yamamoto, T., 2011. Formation and assignment of silver defect centres in phosphate glass induced by femtosecond laser pulses. Radiat. Meas. 46, 1402–1405. https://doi.org/10.1016/j.radmeas.2011.01.004.

Ziegler, J.F., Ziegler, M.D., Biersack, J.P., 2010. SRIM – the stopping and range of ions in matter (2010). Nucl. Instrum. Methods Phys. B 268, 1818–1823. https://doi.org/10.1016/j.nimb.2010.02.091.